Gaussian Layer Connectivity Parameterization: A New Approach to Topology Optimization of Multi-Body Mechanisms

Kenneth E. Swartz[a], Kai A. James[b]

[a]*Department of Mechanical Science and Engineering, University of Illinois, Urbana, IL 61801, USA*
[b]*Department of Aerospace Engineering, University of Illinois, Urbana, IL 61801, USA*

Abstract

Topology optimization is extended to the design of multi-body mechanisms. A Gaussian function is used to parameterize the location of inter-body connections, thereby enabling the optimization of both mass distribution and inter-body connectivity simultaneously. The potential for large rigid-body rotation necessitates the use of a geometrically nonlinear finite element analysis to properly model mechanism response. The unknown displacement field is calculated with a Newton-Raphson iterative scheme. An adjoint analysis is performed to efficiently compute the design sensitivities used in the gradient-based optimization procedure. The proposed technique is demonstrated on the design of multi-body grippers and force/displacement inverters.

Keywords: topology optimization, multi-body mechanism design, nonlinear finite element analysis, adjoint sensitivity analysis

1. Introduction

Topology optimization applies nonlinear programming to algorithmically design optimal structures [1]. Common design problems include compliance minimization subject to a mass constraint [2] and mass minimization subject to a stress constraint [3]. As manufacturing technologies have advanced in recent years, specifically additive manufacturing, the design process has become more important to leverage the potential performance gains that are now possible. For example, multi-scale design is nearly impossible to optimize heuristically based on human intuition and experience. Computational design tools based on mathematical principles provide a much better foundation for complex design problems [4].

Traditionally, a design domain is discretized into a finite number of cells, each of which are assigned a design parameter. The optimal distribution of material, or optimal structure, is then determined by solving the integer programming problem of determining which cells should have material and which cells should not [5]. To facilitate nonlinear programming, the problem is relaxed by allowing continuously varying design parameters. The stiffness of intermediate volume fractions, i.e. those parameters with a value somewhere between solid and void, has been computed using a homogenization technique [1, 6] or a material interpolation scheme [7, 8, 9]. Final designs consisting only of design parameters corresponding to solid or void can be obtained if the material interpolation scheme penalizes the stiffness-to-weight ratio of intermediate design parameters and a resource constraint is employed [5]. Numerical instabilities, such as "checkerboarding", arise from the numerical discretization [10], but may be alleviated with a geometrically limiting constraint, such as a perimeter constraint [11], a slope constraint [12], or a density filter [13].

The vast majority of mechanism design using topology optimization has focused on the design of single-body structures [14], such as compliant mechanisms [15, 16]. However, multi-body structures have been the subject of recent research [17, 18]. Numerical optimization has previously been used to design the topology of flexible, multi-body mechanisms with fixed connections [19] or to design the connectivity of rigid multi-body mechanisms [20, 21, 22, 23]. This work proposes a method to simultaneously optimize the topology and inter-body connectivity of flexible, planar multi-body structures, which serve as an alternative to single-body compliant mechanisms.

Optimizing element connectivity by allowing the stiffness of elastic links connecting elements to vary is not a new approach. Single-body structures have been optimized by parameterizing the element connectivity rather than the element volume fraction to avoid the numerical issues caused by low volume fraction elements [24], and multi-body rigid block linkages have been optimized by parameterizing inter-body elastic links to model revolute joints [25, 26]. The proposed technique extends the idea of optimizing element connectivity by parameterizing inter-body link elements to determine optimal connectivity, while simultaneously parameterizing element volume fractions to determine optimal topology. Previous work by the current authors designated a design parameter to each inter-body link [27], while the present work suggests a way to reduce the number of design parameters utilizing a Gaussian parameterization for inter-body connectivity.

The ability to synthesize multi-body structures without prescribing the

inter-body connectivity a priori would enhance the effectiveness of design algorithms and allow numerical optimization to improve the design process for a new class of complex problems.

Multi-body mechanisms may undergo large motion as they are actuated. To accurately model this motion, specifically rigid-body rotation, a geometrically nonlinear finite element analysis is employed. A linear material model is assumed despite use of the nonlinear Green-St. Venant strain, since the majority of the displacement is expected to be from rigid body rotation about pin joints rather than elastic distortion. The equilibrium displacement field is computed using a Newton-Raphson iterative scheme. A density filter allows local feature size control and avoids the "checkerboard" instability [10]. Optimal multi-body structures are obtained using the method of moving asymptotes (MMA) [28], which requires design sensitivities that are efficiently obtained using the adjoint method.

Section 2 provides the theoretical foundation of the proposed optimization method. Section 3 demonstrates the method on the design on the design of grippers and force/displacement inverters. Multi-body structures with optimal mechanical and geometric advantage are explored.

2. Theory and Methods

Two-dimensional, planar structures are synthesized using a new topology optimization technique. The designs are parameterized using two types of design variables discussed in Section 2.1, modeled using a geometrically nonlinear finite element analysis outlined in Section 2.3, and optimized using the nonlinear programming methodology presented in Section 2.4.

2.1. Design Parameterization

Two-dimensional, planar mechanisms are modeled using multiple coincident finite element meshes. Each of these two-dimensional meshes is referred to as a "layer", and may contain zero, one, or more separate bodies. Each layer is discretized with quadrilaterial, continuum finite elements modeling the elastic bodies and is connected to other layers by linear spring elements, which are used to model pin joints. A visualization of the parameterization of the planar mechanisms is displayed in Figure 1, for an example using 3 layers. In practice, the maximum number of layers must be prescribed before the optimization begins, however the optimizer may use only a fraction of the alotted layers. Note that each mesh actually lies in the same plane, although they are separated in a third dimension for the illustration.

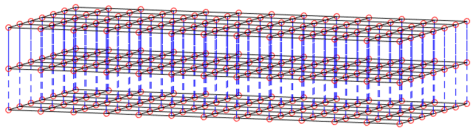

Figure 1: Visualization of element connectivity; ○ nodes, ——body element edges, - - -link elements

Two types of design parameters are used to describe each design, namely, body element stiffness parameters x_{body} and pin joint location parameters x_{link}. The volume fraction of each body element is assigned a x_{body} value that indicates the relatives stiffness of that continuum element. A volume fraction of $x_{\text{body}} \approx 0$ corresponds to void or no material, while a volume fraction of $x_{\text{body}} = 1$ corresponds to solid material. A lower bound of $\rho_{\min} = 1 \times 10^{-3}$ is selected to avoid a singular consistent tangent operator that would result from a truly void element. Body element relative stiffness values are computed according to a SIMP interpolation scheme [7] given by

$$E = E_0 x_{\text{body}}^p, \tag{1}$$

where E is the effective Young's modulus of the element, E_0 is the Young's modulus of the base material, and p is a penalization exponent. This interpolation scheme penalizes intermediate volume fractions by reducing their stiffness-to-weight ratio when $p > 1$, causing the optimizer to select values of $\rho_{\min}$ or 1 when a resource constraint is employed as they are the most economical. The derivative of a body element stiffness with respect to the corresponding volume fraction is given by

$$E = E_0 p x_{\text{body}}^{(p-1)}, \tag{2}$$

which will be needed for the sensitivity analysis performed in Section 2.3.4.

The bodies on separate layers interact through linear elastic springs, or "links", connecting each pair of coincident nodes on prescribed layers. The stiffnesses of these "links" are distributed in such a way to model pin joints; the locations of which (x_{pin}, y_{pin}) are optimized. The stiffness of all link elements k_i is computed by evaluating a Gaussian stiffness distribution at the location of the link element (x_i, y_i), which is given by

$$k_i(x_{\text{pin}}, y_{\text{pin}}) = K_0 \exp\left(-\left(\frac{(x_i - x_{\text{pin}})^2}{2\sigma_x^2} + \frac{(y_i - y_{\text{pin}})^2}{2\sigma_y^2}\right)\right), \tag{3}$$

where K_0 is the nominal stiffness of the pin joint and σ_x and σ_y are the standard deviations of the stiffness distribution in the x and y directions,

respectively. These link elements are assembled into the global finite element system and serve to penalize relative displacement between the two nodes that are connected. This technique aims to approximate the kinematics of a pin joint, as proper selection of σ_x and σ_y will result in relatively high stiffness at nodes near the candidate pin location (x_{pin}, y_{pin}) and relatively low stiffness at surrounding nodes. There will be a nonzero stiffness at each link in the domain, however, far away from the pin location the stiffness is negligible due to the exponential nature of Equation (3). If there are multiple pin joints connecting the same layers, their stiffness contributions can be linearly superposed.

The derivatives of the inter-layer link stiffnesses with respect to the pin coordinates are given by

$$\frac{\partial k_i(x_{\text{pin}}, y_{\text{pin}})}{\partial x_{\text{pin}}} = K_0 \exp\left(-\left(\frac{(x_i - x_{\text{pin}})^2}{2\sigma_x^2} + \frac{(y_i - y_{\text{pin}})^2}{2\sigma_y^2}\right)\right)\left(\frac{(x_i - x_{\text{pin}})}{\sigma_x^2}\right) \tag{4}$$

$$\frac{\partial k_i(x_{\text{pin}}, y_{\text{pin}})}{\partial y_{\text{pin}}} = K_0 \exp\left(-\left(\frac{(x_i - x_{\text{pin}})^2}{2\sigma_x^2} + \frac{(y_i - y_{\text{pin}})^2}{2\sigma_y^2}\right)\right)\left(\frac{(y_i - y_{\text{pin}})}{\sigma_y^2}\right), \tag{5}$$

which will be needed for the sensitivity analysis performed in Section 2.3.4.

2.2. Link Stiffness Estimation

The maximum link stiffness used to represent a pin joint was estimated using a finite element analysis. A linear elastic model was used to calculate the deflection of a three-dimensional cylinder under representative loading in the commercial software ABAQUS. The bottom half of the pin was fixed, while a distributed load of $P = 1\,\text{N}\,\text{m}^{-2}$ was applied to the top half as displayed in Figure 2. The planar mechanisms discussed in Section 3 were assumed to have a thickness of t =10 mm and overall size on the order of ≈ 100 mm. Pins of length $l = 2t$ =20 mm with diameter varying from d =1 mm-5 mm were analyzed to give an estimate and range for realistic pin stiffnesses K_0. The stiffness was computed by dividing the total applied load $F = \frac{Pdl}{2}$ by the displacement x of the midpoint of the top half of the cylinder, which was estimated as half of the displacement of the top of the pin. The results of the calculations are given in Table 1. A K_0 value of $1 \times 10^5\,\text{N}\,\text{mm}^{-1}$ was selected for the optimizations presented in Section 3.

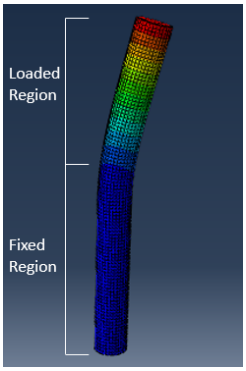

Figure 2: Finite element analysis used to estimate pin stiffness

Table 1: Computed Link Stiffnesses

Diameter (mm)	Length (mm)	F (N)	x (mm)	K_0 ($\mathrm{N\,mm^{-1}}$)
1	20	0.01	6.71×10^{-5}	1.49×10^{2}
2	20	0.02	8.65×10^{-6}	2.31×10^{3}
3	20	0.03	2.71×10^{-6}	1.11×10^{4}
4	20	0.04	1.23×10^{-6}	3.26×10^{4}
5	20	0.05	6.82×10^{-7}	7.34×10^{4}

2.3. Geometrically Nonlinear Finite Element Analysis

Multi-body mechanisms may undergo large motion upon actuation. A geometrically nonlinear finite element analysis is employed to model design responses, since large rotations are not accurately modeled using infinitesimal strain theory. Previous work has revealed that a nonlinear analysis can result in significant performance improvements over a linear analysis [29]. This technique also has the advantage of capturing the load dependence of optimal designs, which has been investigated in previous nonlinear elastic optimizations [13]. The Green-St. Venant strain $\boldsymbol{E}$, defined by

$$\boldsymbol{E} = \frac{1}{2}\left(\boldsymbol{F}^T\boldsymbol{F} - \boldsymbol{I}\right), \tag{6}$$

where $\boldsymbol{F}$ is the deformation gradient and $\boldsymbol{I}$ is the identity tensor, does not produce strain through rigid-body rotations and will thus serve to accurately model large motion. The deformation gradient, which is the derivative of the deformed coordinates $\boldsymbol{X}$ with respect to the original coordinates $\boldsymbol{x}$, can be equivalently expressed as $\boldsymbol{F} = \partial\boldsymbol{X}/\partial\boldsymbol{x}$ or $\boldsymbol{F} = \nabla\boldsymbol{U} + \boldsymbol{I}$, where $\boldsymbol{U}$ is the

displacement field given by $\boldsymbol{U} = \boldsymbol{X} - \boldsymbol{x}$. The strong form of the equilibrium equations expressed over a general domain Ω, such as the one pictured in Figure 3, is given by

$$\nabla \cdot \boldsymbol{F}\boldsymbol{S} + \boldsymbol{b} = 0 \in \Omega \tag{7}$$

$$\boldsymbol{U} = \boldsymbol{U}^p \in A^u \tag{8}$$

$$\boldsymbol{F}\boldsymbol{S}\boldsymbol{n} = \boldsymbol{t}^p \in A^t, \tag{9}$$

where $\nabla\cdot$ is the divergence operator, $\boldsymbol{S}$ is the Second Piola-Kirchoff stress, $\boldsymbol{b}$ is the body force per unit volume, $\boldsymbol{U}^p$ are the prescribed displacements which are applied to the fixed boundary region A^u, n is the unit normal vector, and $\boldsymbol{t}^p$ are the prescribed tractions which are applied to the boundary region A^t. Equations (7)-(9) are expressed in an equivalent weak form given by

$$\int_\Omega \boldsymbol{w} \cdot (\nabla \cdot \boldsymbol{F}\boldsymbol{S} + \boldsymbol{b})\,\mathrm{d}\Omega + \int_{A^t} \boldsymbol{w} \cdot (\boldsymbol{F}\boldsymbol{S}\boldsymbol{n} - \boldsymbol{t}^p)\,\mathrm{d}A^t = 0, \tag{10}$$

where $\boldsymbol{w}$ are weighting functions. Integration by parts and the divergence theorem are applied to recast Equation (10) into a form suitable for discretization by the Galerkin finite element method [30].

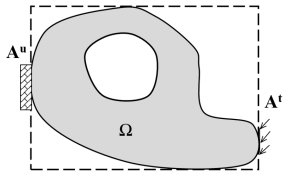

Figure 3: Boundary value problem domain

A linear elastic material model is assumed, with a constitutive relation given by

$$\boldsymbol{S} = \boldsymbol{C}\boldsymbol{E}, \tag{11}$$

where $\boldsymbol{C}$ is the constitutive tensor which is independent of displacement. This model is motivated by the expectation that multi-body mechanisms may undergo large displacements, yet small strains. The inclusion of pin joints will allow large relative rotations to take place between bodies without large material distortions.

2.3.1. Newton-Raphson Solution Procedure

The iterative Newton-Raphson method is used to calculate equilibrium displacement solutions $\boldsymbol{U}$ that satisfy

$$\boldsymbol{R}(\boldsymbol{U}) = \boldsymbol{F}_{\text{ext}} - \boldsymbol{F}_{\text{int}}(\boldsymbol{U}) = 0, \tag{12}$$

where $\boldsymbol{R}(\boldsymbol{U})$ is the residual vector that is to be minimized. The external force vector, $\boldsymbol{F}_{\text{ext}}$, and internal force vector, $\boldsymbol{F}_{\text{int}}(\boldsymbol{U})$, are deduced from Equation (10). A first-order Taylor series approximation is used to compute the displacement update $\Delta\boldsymbol{U}$ at each iteration i that causes the residual to be zero, or $\boldsymbol{R}(\boldsymbol{U}_i + \Delta\boldsymbol{U}) = 0$. The displacement update is calculated according to

$$\boldsymbol{K}(\boldsymbol{U}_i)\,\Delta\boldsymbol{U} = \boldsymbol{R}(\boldsymbol{U}_i)\,, \tag{13}$$

where $\boldsymbol{K}$ is the consistent tangent operator defined as $\boldsymbol{K}(\boldsymbol{U}_i) = -\frac{\partial \boldsymbol{F}_{\text{int}}(\boldsymbol{U}_i)}{\partial \boldsymbol{U}_i}$. The displacement solution is updated each iteration by $\boldsymbol{U}_{i+1} = \boldsymbol{U}_i + \Delta\boldsymbol{U}$. This iterative process continues until Equation (12) converges to within a satisfactory tolerance.

2.3.2. Displacement Damping

Dirichlet boundary conditions are necessary to obtain a non-singular consistent tangent operator and find a unique solution to the unknown displacement field. Proper selection of boundary conditions proved to be a challenge in the multi-body framework as there were multiple meshes to constrain and the function of each layer was not known a priori. Adequate boundary conditions often overly restricted the design, and so "anchor springs" were attached to act as displacement dampers. All nodes in each layer were attached to a fixed node (i.e. a node with a Dirichlet boundary condition of zero displacement) by linear spring elements with relatively low stiffness. With sufficient "anchor spring"stiffness, or displacement damping, the solution could converge under Dirichlet boundary conditions that would otherwise contain rigid body displacement modes.

It was often observed in practice that the pin joints between layers removed the rigid body displacement modes, thus adequately constraining the multi-body mesh. However, the optimization was prone to instability and divergence if regions of the design space exist where the mesh was not constrained properly. The inclusion of displacement damping resolved this issue and allowed the optimization to progress. "Anchor spring" stiffnesses are provided in Section 3.

2.3.3. Density Filtering

For a given volume fraction, a structure with more smaller holes is stiffer than a structure with fewer larger holes [10]. An ill-posed optimization problem therefore results from a finite element discretization, as optimal designs are a function of the mesh resolution; the optimizer will create smaller features as the mesh is refined. This "checkerboard" instability can be rectified

by including a geometrically limiting constraint. A density filter that penalizes designs with features smaller than the filter radius is employed to create a well-posed optimization problem.

Filtered volume fractions x_{body}, which are used in the finite element analysis, are computed as a function of unfiltered volume fractions $\bar{x}_{\text{body}}$, which are the independent design variables. Their relation is given in matrix form by

$$\boldsymbol{x}_{\mathbf{body}} = \boldsymbol{W}\bar{\boldsymbol{x}}_{\mathbf{body}}. \tag{14}$$

where $\boldsymbol{W}$ is the filtering matrix [13]. The components of $\boldsymbol{W}$ are determined by first computing $\tilde{\boldsymbol{W}}$ according to

$$\tilde{W}_{i,j} = \max(0, \varepsilon - d_{i,j}), \tag{15}$$

where ε is the filter radius and $d_{i,j}$ is the distance between elements i and j. Each row of $\tilde{\boldsymbol{W}}$ is normalized to obtain $\boldsymbol{W}$, ensuring that filtered volume fractions are in the range of 0 and 1.

2.3.4. Adjoint Sensitivity Analysis

An adjoint analysis is used to compute the sensivities of response functions with respect to the design parameters. The adjoint expressions are derived as follows. Consider a general response function of the form

$$f = \Pi(\boldsymbol{U}(\boldsymbol{x}), \boldsymbol{P}(\boldsymbol{x}), \boldsymbol{x}), \tag{16}$$

where $\boldsymbol{U}$ is the vector of all nodal displacements, $\boldsymbol{P}$ is the vector of all nodal forces, and $\boldsymbol{x}$ is the vector of design parameters. The derivative of Equation (16) for response functions containing unknown displacements $\boldsymbol{U}^{\text{f}}$ and unknown reaction forces $\boldsymbol{P}^{\text{p}}$ will contain implicit derivatives that are expensive to compute. The superscripts f and p denote the partitions of the finite element vectors which correspond to degrees of freedom with free and prescribed displacements, respectively. The adjoint method permits the removal of these implicit terms from the sensitivity expression and is computationally advantageous over a direct method for optimization problems containing more design variables than constraint functions. Equation 16 can be re-written as

$$f = \Pi(\boldsymbol{U}(\boldsymbol{x}), \boldsymbol{P}(\boldsymbol{x}), \boldsymbol{x}) + \boldsymbol{\lambda}^{\text{T}}\boldsymbol{R}, \tag{17}$$

where $\boldsymbol{R}$ is the residual vector and $\boldsymbol{\lambda}$ is an arbitrary constant vector, since the addition of zero will not change the right hand side and the inner product of any vector with the zero vector will remain zero. The accuracy of

the sensitivities are therefore reliant upon the tolerance of the linear solution obtained from the Newton-Raphson procedure, as the residual vector is assumed here to be zero. Differentiating Equation (17) with respect to a particular design parameter under the assumption of design independent loading gives a sensitivity expression via the chain rule of

$$\frac{d\Pi}{dx} = \frac{\partial \Pi}{\partial \boldsymbol{U}^{\mathrm{f}}} \frac{d\boldsymbol{U}^{\mathrm{f}}}{dx} + \frac{\partial \Pi}{\partial \boldsymbol{P}^{\mathrm{p}}} \frac{d\boldsymbol{P}^{\mathrm{p}}}{dx} + \frac{\partial \Pi}{\partial x} + \boldsymbol{\lambda}^{\mathrm{f}\,\mathrm{T}} \frac{d\boldsymbol{R}^{\mathrm{f}}}{dx} + \boldsymbol{\lambda}^{\mathrm{p}\,\mathrm{T}} \frac{d\boldsymbol{R}^{\mathrm{p}}}{dx}. \tag{18}$$

Derivatives with respect to body element parameters refer to filtered volume fractions, although derivative with respect to unfiltered volume fractions can be easily obtained by differentiating Equation (14) and employing the chain rule.

Two types of functions will be considered here and will serve to form a basis for all objective and constraint functions. The first response function is of the form

$$f_1 = \boldsymbol{L}^{\mathrm{f}\,\mathrm{T}} \boldsymbol{U}^{\mathrm{f}}, \tag{19}$$

where $\boldsymbol{L}^{\mathrm{f}}$ is a constant vector used to define a response function involving unknown displacements. Selecting the prescribed and free partitions of the arbitrary vector, $\boldsymbol{\lambda}$, such that

$$\boldsymbol{\lambda}^{\mathrm{p}} = \boldsymbol{0} \qquad \boldsymbol{\lambda}^{\mathrm{f}} = \boldsymbol{K}^{\mathrm{ff}\,-1} \boldsymbol{L}^{\mathrm{f}}, \tag{20}$$

reduces the sensitivity expression to

$$\frac{d\Pi}{dx} = -\boldsymbol{\lambda}^{\mathrm{f}\,\mathrm{T}} \frac{\partial \boldsymbol{F}^{\mathrm{f}}_{\mathrm{int}}}{\partial x} = -\left(\boldsymbol{K}^{\mathrm{ff}\,-1} \boldsymbol{L}^{\mathrm{f}}\right)^{\mathrm{T}} \frac{\partial \boldsymbol{F}^{\mathrm{f}}_{\mathrm{int}}}{\partial x}. \tag{21}$$

Note that when $\boldsymbol{L}^{\mathrm{f}} = \boldsymbol{P}^{\mathrm{f}}$, i.e. the response function is the compliance, there is no need to solve a new linear system for the adjoint vector as $\boldsymbol{\lambda}^{\mathrm{f}} = \boldsymbol{U}^{\mathrm{f}}$.

The second response function is of the form

$$f_2 = \boldsymbol{L}^{\mathrm{p}\,\mathrm{T}} \boldsymbol{P}^{\mathrm{p}}, \tag{22}$$

where $\boldsymbol{L}^{\mathrm{p}}$ is a vector used to define a response function involving reaction forces. Selecting the prescribed and free partitions of the arbitrary vector, $\boldsymbol{\lambda}$, such that

$$\boldsymbol{\lambda}^{\mathrm{p}} = -\boldsymbol{L}^{\mathrm{p}} \qquad \boldsymbol{\lambda}^{\mathrm{f}} = -\boldsymbol{K}^{\mathrm{ff}\,-1} \left(\boldsymbol{K}^{\mathrm{fp}} \boldsymbol{L}^{\mathrm{p}}\right), \tag{23}$$

reduces the sensitivity expression to

$$\frac{d\Pi}{dx} = -\boldsymbol{\lambda}^{\mathrm{f}\,\mathrm{T}} \frac{\partial \boldsymbol{F}^{\mathrm{f}}_{\mathrm{int}}}{\partial x} - \boldsymbol{\lambda}^{\mathrm{p}\,\mathrm{T}} \frac{\partial \boldsymbol{F}^{\mathrm{p}}_{\mathrm{int}}}{\partial x} = -\left(\boldsymbol{K}^{\mathrm{ff}\,-1} \left(\boldsymbol{K}^{\mathrm{fp}} \boldsymbol{L}^{\mathrm{p}}\right)\right)^{\mathrm{T}} \frac{\partial \boldsymbol{F}^{\mathrm{f}}_{\mathrm{int}}}{\partial x} - (\boldsymbol{L}^{\mathrm{p}})^{\mathrm{T}} \frac{\partial \boldsymbol{F}^{\mathrm{p}}_{\mathrm{int}}}{\partial x}. \tag{24}$$

By selecting the above-defined adjoint solution for each function of interest, we cause all therms containing implicit derivatives to vanish from the sensitivity expression, thereby increasing the computational efficiency of the sensitivity calculation. The explicit derivatives of the internal force vector with respect to the design parameters, $\frac{\partial \boldsymbol{F}_{\text{int}}^{\text{f}}}{\partial x}$, can be obtained with the help of Equations (2), (4), and (5).

2.4. Optimization Problem

Nonlinear programming is used to solve optimization problems of the form

$$\begin{aligned} \underset{\boldsymbol{x}}{\text{minimize}} \quad & f(\boldsymbol{x}) \\ \text{subject to} \quad & g_i(\boldsymbol{x}) \leq 0, && i = 1, 2, ...N_{\text{constraint}} \\ & x_{\min j} \leq x_j \leq x_{\max j}, && j = 1, 2, ...N_{\text{param}} \end{aligned} \tag{25}$$

where $\boldsymbol{x}$ is the vector of design parameters, $f(\boldsymbol{x})$ is the objective function, $g_i(\boldsymbol{x})$ are the constraint functions, and $x_{\min j}$ and $x_{\max j}$ denote the lower and upper bounds for each design parameter x_j. All numerical optimizations in this work were solved using the method of moving asymptotes (MMA) [28]. The inclusion of step limits for the pin location parameters was necessary to reduce the norm of the KKT conditions to a suitable tolerance. This will be discussed in further detail in Section 3.

Two design problems will be addressed. The first is that of mechanical advantage, or the ratio of output force F_{out} to input force F_{in}. The formal optimization problem is given by

$$\begin{aligned} \underset{\boldsymbol{x}}{\text{minimize}} \quad & \frac{-F_{\text{out}}}{F_{\text{in}}} = \frac{\boldsymbol{L}^{\text{p}\,\text{T}} \boldsymbol{P}^{\text{p}}}{\boldsymbol{L}^{\text{f}\,\text{T}} \boldsymbol{P}^{\text{f}}} \\ \text{subject to} \quad & \boldsymbol{R}(\boldsymbol{U}) = 0 \\ & \boldsymbol{U} = \boldsymbol{U}^p \in A^u \\ & \boldsymbol{F}\boldsymbol{S}\boldsymbol{n} = \boldsymbol{t}^p \in A^t \\ & C = \boldsymbol{P}^{\text{f}\,\text{T}} \boldsymbol{U}^{\text{f}} \leq C_{\max} \\ & \frac{1}{N_{\text{body}\,k}} \sum_{j=1}^{N_{\text{body}\,k}} x_{\text{body}\,j} \leq V_{\max k} \\ & \rho_{\min} \leq x_{\text{body}\,m} \leq 1 \qquad m = 1, 2, ...N_{\text{body}} \\ & z_{\min} \leq x_{\text{link}\,n} \leq z_{\max} \qquad n = 1, 2, ...N_{\text{link}}, \end{aligned} \tag{26}$$

where $\boldsymbol{L}^{\mathrm{p}}$ is a vector defined here to select desired reaction forces, $\boldsymbol{L}^{\mathrm{f}}$ is a vector defined here to select desired input forces, C is the compliance of the structure, N_{body_k} is the number of body elements on a given layer k, $V_{\mathrm{max}k}$ is the maximum volume fraction of layer k, and z_{min} and z_{max} are domain specific bounds on pin location. A maximum compliance C_{max} constraint is necessary to ensure that the structure has a requisite level of stiffness.

The second design problem studied is that of geometric advantage, or the ratio of output displacement U_{out} to input displacement U_{in}. The formal optimization problem is given by

$$
\begin{aligned}
\underset{\boldsymbol{x}}{\text{minimize}} \quad & \frac{-U_{\mathrm{out}}}{U_{\mathrm{in}}} = \frac{\boldsymbol{L}^{\mathrm{f}\,\mathrm{T}}\boldsymbol{U}^{\mathrm{f}}}{\boldsymbol{L}^{\mathrm{p}\,\mathrm{T}}\boldsymbol{U}^{\mathrm{p}}} \\
\text{subject to} \quad & \boldsymbol{R}(\boldsymbol{U}) = 0 \\
& \boldsymbol{U} = \boldsymbol{U}^{p} \in A^{u} \\
& \boldsymbol{F}\boldsymbol{S}\boldsymbol{n} = \boldsymbol{t}^{p} \in A^{t} \\
& F_{\mathrm{in}} = \boldsymbol{L}^{\mathrm{p}\,\mathrm{T}}\boldsymbol{P}^{\mathrm{p}} \geq F_{\mathrm{min}} \\
& \frac{1}{N_{\mathrm{body}_k}} \sum_{j=1}^{N_{\mathrm{body}_k}} x_{\mathrm{body}_j} \leq V_{\mathrm{max}k} \\
& \rho_{\mathrm{min}} \leq x_{\mathrm{body}_m} \leq 1 \qquad m = 1, 2, ...N_{\mathrm{body}} \\
& z_{\mathrm{min}} \leq x_{\mathrm{link}n} \leq z_{\mathrm{max}} \qquad n = 1, 2, ...N_{\mathrm{link}}
\end{aligned}
\tag{27}
$$

where $\boldsymbol{L}^{\mathrm{p}}$ is a vector defined here to select desired input displacements, $\boldsymbol{L}^{\mathrm{f}}$ is a vector defined here to select desired output displacements. For certain boundary conditions a minimum force F_{min} may need to be enforced to achieve reasonable designs. A maximum force may be imposed in place of or in addition to a minimum force if needed for the application.

3. Results and Discussion

Two common topology optimization design problems are explored in a multi-body framework. First, a gripper is synthesized using two layers to display the method's ability to optimize material distribution and inter-body connectivity simultaneously. The optimal designs for mechanical advantage and geometric advantage are computed for a range of input parameters. The second design problem investigated is that of a force or displacement inverter. Optimal designs are computed for mechanical advantage, corresponding to a force inverter, and geometric advantage, corresponding to

a displacement inverter, on a design domain consisting of 3 body element layers.

3.1. Multi-Body Gripper Design Conditions

A common example problem in traditional, single-body topology optimization is that of a compliant gripper mechanism. The basic function is to magnify input displacements or forces to gain a geometric or mechanical advantage, respectively. An example compliant gripper optimized for mechanical advantage is presented in Figure 4. This mechanism relies on elastic distortion for actuation and would not function at all if the material were perfectly rigid. Despite the simplicity of a single part, this design has the disadvantage that energy is lost to elastic distortion and it may be susceptible to fatigue due to the flexural hinges that create stress concentrations [16].

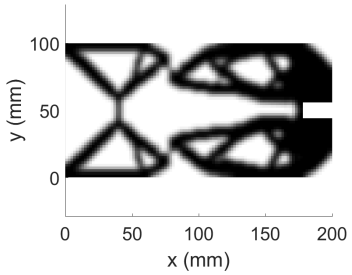

Figure 4: Example compliant gripper design

The proposed method aims to design a gripper that utilizes a pin joint, rather than elastic distortion, to increase mechanical efficiency and reduce material fatigue. The multi-body design domain consists of two body element layers connected by one link element layer with one Gaussian modeled pin joint, which is initialized to $(x, y) = (90, 50)$. In all optimizations, an initial volume fraction equal to the maximum volume fraction constraint is applied to each element on each layer. The gripper is actuated with equal and opposite vertical forces or displacements on the left side of the domain, while output forces or displacements are desired at a prescribed location on the left side of the domain, as pictured in Figure 5.

Symmetry was imposed between the two layers by associating the volume fraction of mirrored elements in opposing layers with the same design parameter. For example, the volume fraction of the element in the top left corner of layer 1 corresponded to the same design parameter as the volume fraction of the element in the bottom left corner of layer 2. Enforcing

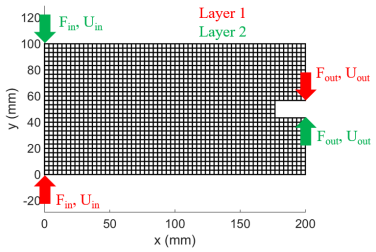

Figure 5: Domain and boundary conditions for the gripper design problem

symmetry reduced the dimensionality of the numerical optimization problem therefore reducing computational cost, and ensured the grippers were ambidextrous, which is advantageous for manufacturing and usage.

The parameters used in the multi-body optimizations are presented in Table 2. Parameters specific to the gripper design problem are presented in Table 3. Note that the input displacement only applies to the geometric advantage optimization, and the input force only applies to the mechanical advantage optimization. Additionally, the output spring stiffness has no bearing on mechanical advantage results as the output node is fixed. A maximum volume fraction is imposed on each layer, and the reported total maximum volume fraction in Table 3 is a sum of all layer maximum volume fractions.

Input displacements are applied through Dirichlet boundary conditions, and input forces are applied through Neumann boundary conditions. Output displacements were obtained by computing the displacement at desired nodes, although it should be noted that in practice a spring was connected between output nodes and a fixed node to require material be present at the output location. The displacement of a node attached to a spring is analogous to output force in a linear finite element analysis, however, the use of a spring with relatively low stiffness and a geometrically nonlinear finite element analysis justify this definition of output displacement in the current work. Output forces were obtained by fixing the desired nodes with Dirichlet boundary conditions and computing the associated reaction forces.

The use of a Gaussian distribution of stiffness to model a pin joint will affect the accuracy of the design evaluations. The non-zero stiffness at neighboring nodes, which allowed the pin joint to migrate throughout the domain without falling into local minima, will not behave the same as a pin joint with zero rotational stiffness. The standard deviations were set to the same length as the node spacing, or $\sigma_x = \sigma_y = \Delta_x = \frac{L_x}{(N_x - 1)}$. If the Gaussian

Table 2: Multi-Body Mechanism Optimization Conditions

Description	Symbol	Value
Sum of Anchor Spring Stiffnesses	k_{anch}	$1 \times 10^2\,\text{N}\,\text{mm}^{-1}$
Output Spring Stiffnesses	k_{out}	$1 \times 10^4\,\text{N}\,\text{mm}^{-1}$
Maximum Link Stiffness	K_0	$1 \times 10^5\,\text{N}\,\text{mm}^{-1}$
Link Standard Deviation	σ_x, σ_y	2 mm
Young's Modulus	E_0	200 GPa
Poisson's Ratio	ν	0.3
Minimum Volume Fraction	$x_{\min}$	1×10^{-3}
Maximum Volume Fraction	$x_{\max}$	1.0
SIMP Penalty Exponent	p	3
Density Filter Radius	ε	5 mm
Domain Thickness	t	10 mm
Input Force Magnitude	F_{in}	$1 \times 10^2\,\text{N}$
Input Displacement Magnitude	U_{in}	$1 \times 10^{-2}\,\text{mm}$

Table 3: Gripper Design Specific Conditions

Description	Symbol	Value
Domain Length	L_x	200 mm
Domain Height	L_y	100 mm
Number of Nodes in x-direction	N_x	101
Number of Nodes in y-direction	N_y	51
Maximum Total Volume Fraction	$V_{\text{total,max}}$	0.75
Maximum Compliance	$C_{\max}$	2 N mm

stiffness distribution was located exactly at a particular node, the closest node (one grid spacing away) would have 61% of the maximum stiffness. The performance accuracy will be estimated by comparing the calculated mechanical advantage of grippers with the theoretical mechanical advantage that comes from the statics problem based only on pin joint location, i.e. equating moments caused by input and output forces.

3.2. Multi-Body Gripper Numerical Results

The gripper design problems aim to determine both the optimal distribution of material along with the optimal pin coordinates. A design optimizing geometric advantage is presented in Figure 6. This design is not typical of everyday pliers, as the optimal pin joint location, $(x_0^*, y_0^*) = (32.5, 50.0)$, is much closer to the input locations than the output locations. However,

it is intuitive to see that small input displacements would be magnified by this pin joint location, thus creating large output displacements. This design achieved a geometric advantage of 1.51, further justifying the technique used to obtain output displacements discussed in Section 3.1. An optimal pin joint location much closer to the output locations would be expected if the inclusion of springs attached to output nodes were erroneously modeling output force. The design in Figure 6 stored 10.0 N mm of strain energy under the loading conditions used for the optimization, which was a significant reduction from 14.3 N mm of stored strain energy in a single-body compliant mechanism optimized under the same parameters.

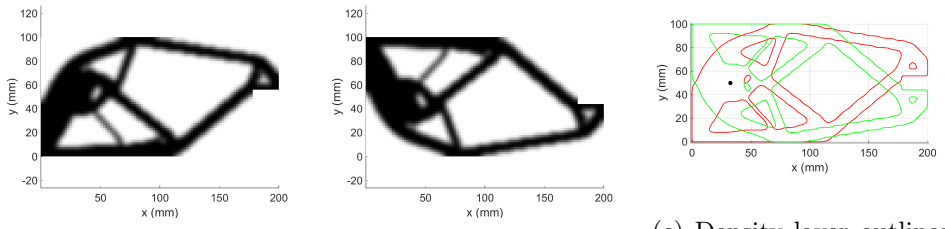

(a) Layer 1 (b) Layer 2 (c) Density layer outlines; • pin joint location

Figure 6: Optimal geometric advantage two-layer gripper

Optimizing mechanical advantage required an additional response constraint. As mentioned in Section 2.4, a compliance constraint is necessary to ensure the structure has a requisite level of stiffness. Absent this constraint the optimizer will almost certainly remove material from the input location, and the resulting singular tangent operator will cause the optimization to fail. Grippers with optimal mechanical advantage subject to a compliance constraint are presented in Figure 7. As expected, the optimal pin joint location, $(x_0^*, y_0^*) = (139.6, 50.0)$, is now closer to the output location than the input location. If the compliance constraint is relaxed x_0^* will increase, and if the compliance constraint is tightened x_0^* will decrease. If we assume that the body is perfectly rigid, the theoretical mechanical advantage can be computed by equating the moments caused by the input and output forces, or $F_{\text{in}}(x_0^*) = F_{\text{out}}(L_x - x_0^*)$. Thus, the mechanical advantage is computed as $F_{\text{out}}/F_{\text{in}} = x_0^*/(L_x - x_0^*)$, which gives a value of 2.31 for the design in Figure 7. The optimal mechanical advantage computed with the Gaussian stiffness pin model was 2.26, or about 2% different than the theoretical response. The difference between the theoretical response and the computed response is due the fact that a portion of the work imparted to

the mechanism by the user, is lost as stored elastic strain energy. The design in Figure 7 stored 1.81 N mm of strain energy under the loading conditions used for the optimization, which was a reduction from 2.00 N mm of stored strain energy in a single-body optimized compliant mechanism optimized under the same parameters.

Iteration histories are provided for the grippers optimized for mechanical advantage. The density fields are displayed in Figure 8, while the mechanical advantage and KKT norm are displayed in Figure 9. The KKT norm was reduced 3 orders of magnitude in 38 MMA iterations, during which the mechanical advantage increased from less than 1.0 in the initial configuration to its final value of 2.26.

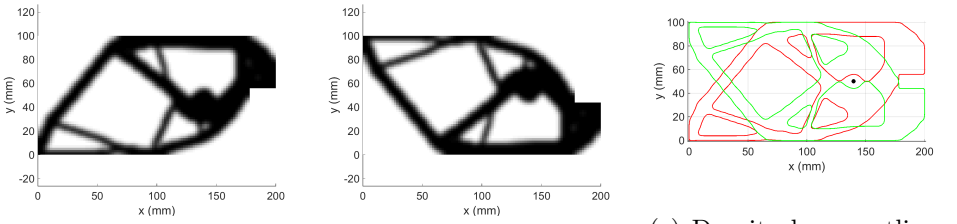

(a) Layer 1 (b) Layer 2 (c) Density layer outlines; • pin joint location

Figure 7: Optimal mechanical advantage two-layer gripper

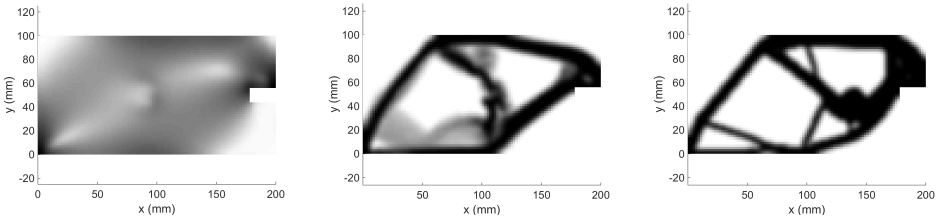

(a) Iteration 1 (b) Iteration 10 (c) Iteration 38

Figure 8: Iteration history of layer 1 density field

The mechanical advantage design problem has inherently small displacements. Fixing the output location is equivalent to putting a very stiff object in the grips of a set of pliers, which restricts all motion except for elastic distortion. For relatively small input forces, or those assumed to be applied by human hands on a steel set of pliers, there will be very small displacements. The geometric advantage design problem, however, lends itself to

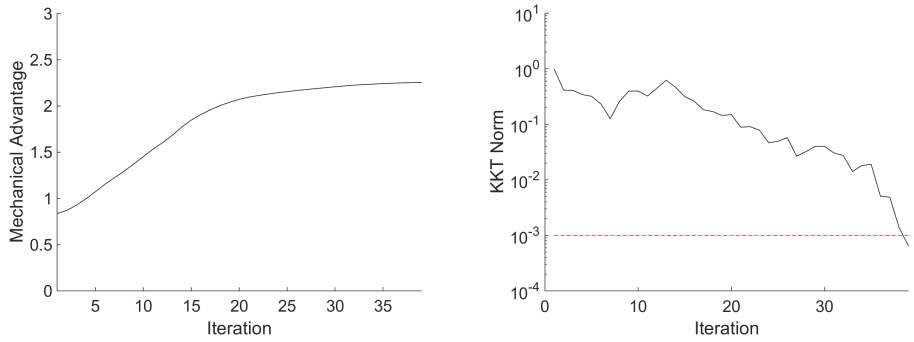

(a) Mechanical advantage (b) KKT norm

Figure 9: Iteration histories

much larger displacements. The output location is allowed to move, which means rigid body rotations are admissible. Despite this, the applied input displacement was only 1×10^{-1} mm, or 0.1% of the domain height. This small value was selected for numerical reasons. The inclusion of void elements in the finite element analysis can result in poor behavior when these low volume fraction elements are distorted. This problem has been addressed previously be removing void elements [31], however a simpler technique of applying small input displacements to avoid the numerical instabilities was employed here.

Solutions were considered optimal once the Karush-Kuhn-Tucker (KKT) conditions [32] had converged to a tolerance of 1×10^{-3}, which was about 3 orders of magnitude lower than the initial KKT norm. As previously mentioned, step limits were imposed on the pin joint location parameters. Specifically, maximum step sizes per iteration of 2% of the parameter range were enforced to prevent oscillation of the pin location and promote stable convergence.

3.3. Force/Displacement Inverter Design Conditions

A force or displacement inverter is another common example problem in single-body topology optimization. The basic function of the mechanism is to change the direction of input forces or displacements by 180°. An example single-body compliant design which maximized mechanical advantage is displayed in Figure 10. As with the gripper, the proposed method aims to design an inverter that utilizes multiple bodies and pin joints to increase efficiency and reduce material fatigue.

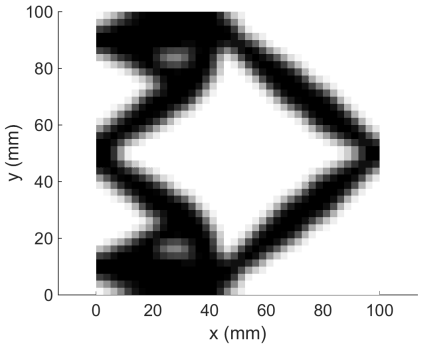

Figure 10: Example compliant force inverter design

Design problems will be solved on computational domains consisting of three body element layers, with two layers of link elements (connecting layers 1 to 2 and layers 2 to 3). The locations of the two pins connecting layers 1 to 2 are initialized to $(x, y) = (40, 40)$ and $(40, 60)$, while the locations of the two pin pins connecting layers 2 to 3 are initialized to $(x, y) = (60, 40)$ and $(60, 60)$. No symmetries were enforced on this domain. The inverter is actuated by a horizontal input force or displacement on the left side of the domain, while a horizontal output force or displacement in the opposite direction is desired at a prescribed location on the left side of the domain, as pictured in Figure 11.

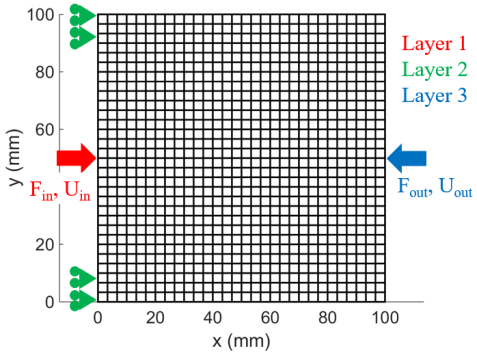

Figure 11: Domain and boundary conditions for the inverter design problem

The parameters specific to multi-body inverter optimizations are listed in Table 4. The parameters listed in Table 2 are also applicable. Again, note that input displacement only applies to the geometric advantage problem, input force only applies to the mechanical advantage problem, and the

Table 4: Displacement/Force Inverter Design Specific Conditions

Description	Symbol	Value
Domain Length	L_x	100 mm
Domain Height	L_y	100 mm
Number of Nodes in x-direction	N_x	51
Number of Nodes in y-direction	N_y	51
Maximum Volume Fraction	$V_{\max}$	0.3
Maximum Compliance	$C_{\max}$	0.5 N mm

output spring stiffness has no bearing on mechanical advantage results. The same techniques for input and output displacement and force discussed in Section 3.1 are employed.

3.3.1. Force/Displacement Inverter Numerical Results

Optimal displacement inverters are pictured in Figure 12, and optimal force inverters are pictured in Figure 13. An encouraging result seen in both Figures 12 and 13 is that multiple distinct bodies can form on the same layer. Specifically, layer 2 in both designs contains two bodies near the fixed boundary conditions. This capability could greatly reduce the dimensionality of multi-body mechanisms by reducing the required number of layers needed to represent them.

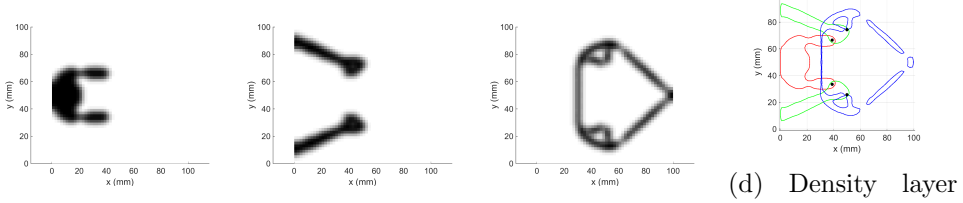

(a) Layer 1 (b) Layer 2 (c) Layer 3 (d) Density layer outlines; • pin joint locations

Figure 12: Optimal three-body displacement inverter

The current designs rely on a combination of elastic distortion and rigid body rotation to achieve motion, however, the amount of material fatigue is reduced by replacing some of the elastic hinges with pin joints. The displacement inverters achieved a geometric advantage of 0.87, and the force inverters achieved a mechanical advantage of 1.59. There are no theoretical values to compare with due to the elastic distortion required for actuation.

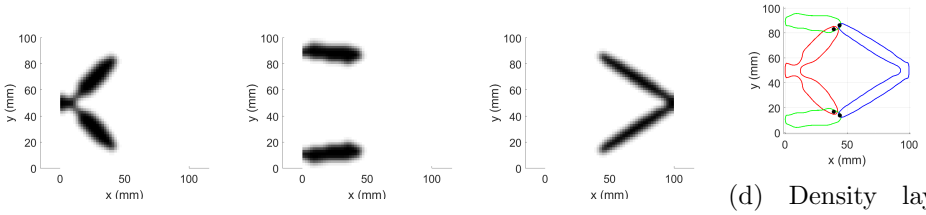

(a) Layer 1 (b) Layer 2 (c) Layer 3 (d) Density layer outlines; • pin joint locations

Figure 13: Optimal three-body force inverter

The inverter optimized for geometric advantage, pictured in Figure 12, has a layer (3) in which four elastic hinges form. The geometric advantage objective function does not take compliance into account, so designs that rely on elastic distortion to achieve large output displacements are not penalized. Large input forces may be necessary to create this motion, but the design's performance is not hindered according to the response functions.

Solutions were once again considered optimal once the KKT conditions had converged to a tolerance of 1×10^{-3}. Step limits of 2% of the parameter range were sufficient to reduce the KKT norm for the mechanical advantage inverter problem. For the inverter optimized for geometric advantage, the step limit was reduced by an order of magnitude to 0.2% of the parameter range to prevent oscillations and ensure convergence.

4. Conclusion

A method is proposed to optimize multi-body mechanisms via topology optimization. The added value over traditional topology optimization comes from the increased design space of multiple bodies connected with optimal connections. Pin joints are modeled by a Gaussian distribution of stiffness and allowed to migrate through the domain until an optimal combination of material distribution and pin joint location is determined. In other words, the connectivity is not defined a priori. Anchoring springs serve to adequately damp displacements to facilitate the nonlinear finite element solution.

Two-body grippers are optimized for both geometric and mechanical advantage. The theoretical mechanical advantage that is computed assuming rigid body rotation only is compared with the final mechanical advantage from the optimization. Numerical results indicate that there is strong

agreement between the two responses, therefore the damping and Gaussian stiffness approximations do not unduly alter the design problem.

Force/displacement inverters are synthesized using a 3-layer design domain. Both results showed that multiple distinct bodies could form on the same layer, which could significantly reduce the dimensionality of the optimization problem as the number of layers are increased in more complicated problems. The optimal designs for geometric and mechanical advantage both use a combination of rigid body rotation and elastic distortion to achieve optimal performance, although the amount of elastic distortion is reduced compared with a single-body design.

5. Acknowledgment

Portions of this work were performed under the auspices of the U.S. Department of Energy by Lawrence Livermore National Laboratory (LLNL) under Contract DE-AC52-07NA27344, cf. ref number LLNL-CONF-717659.

6. References

[1] M. Bendsøe and N. Kikuchi, "Generating optimal topologies in structural design using a homogenization method," *Computer Methods in Applied Mechanics and Engineering*, vol. 71, no. 2, pp. 197–224, 1988.

[2] O. Sigmund, "A 99 line topology optimization code written in matlab," *Structural and Multidisciplinary Optimization*, vol. 21, no. 2, pp. 120–127, 2001.

[3] J. Pereira, E. Fancello, and C. Barcellos, "Topology optimization of continuum structures with material failure constraints," *Structural and Multidisciplinary Optimization*, vol. 26, no. 1-2, pp. 50–66, 2004.

[4] S. Hollister, "Porous scaffold design for tissue engineering," *Nature Materials*, vol. 4, no. 7, pp. 518–524, 2006.

[5] M. P. Bendsøe and O. Sigmund, *Topology Optimization: Theory, Methods, and Applications*. Springer-Verlag Berlin Heidelberg, 2 ed., 2004.

[6] K. Suzuki and N. Kikuchi, "A homogenization method for shape and topology optimization," *Computer Methods in Applied Mechanics and Engineering*, vol. 93, no. 3, pp. 291–318, 1991.

[7] M. P. Bendsøe, "Optimal shape design as a material distribution problem," *Structural optimization*, vol. 1, no. 4, pp. 193–202, 1989.

[8] M. Stolpe and K. Svanberg, "An alternative interpolation scheme for minimum compliance topology optimization," *Structural and Multidisciplinary Optimization*, vol. 22, no. 2, pp. 116–124, 2001.

[9] M. P. Bendsøe and O. Sigmund, "Material interpolation schemes in topology optimization," *Archive of Applied Mechanics*, vol. 69, no. 9, pp. 635–654, 1999.

[10] O. Sigmund and J. Petersson, "Numerical instabilities in topology optimization: A survey on procedures dealing with checkerboards, mesh-dependencies and local minima," *Structural optimization*, vol. 16, no. 1, pp. 68–75, 1998.

[11] R. B. Haber, C. S. Jog, and M. P. Bendsøe, "A new approach to variable-topology shape design using a constraint on perimeter," *Structural optimization*, vol. 11, no. 1, pp. 1–12, 1996.

[12] J. Peterssson and O. Sigmund, "Slope constrained topology optimization," *Numerical Methods in Engineering*, vol. 41, no. 8, pp. 1417–1434, 1998.

[13] T. E. Bruns and D. Tortorelli, "Topology optimization of non-linear elastic structures and compliant mechanisms," *Computer Methods in Applied Mechanics and Engineering*, vol. 190, no. 26-27, pp. 3443–3459, 2001.

[14] X. Guo, W. Zhang, J. Zhang, and J. Yuan, "Explicit structural topology optimization based on moving morphable components (mmc) with curved skeletons," *Computer Methods in Applied Mechanics and Engineering*, vol. 310, pp. 711–748, 2016.

[15] B. Zhu, Q. Chen, J. Mohui, and X. Zhang, "Design of fully decoupled compliant mechanisms with multiple degrees of freedom using topology optimization," *Mechanism and Machine Theory*, vol. 126, pp. 413–428, 2018.

[16] X. Zhang and B. Zhu, *Topology Optimization of Compliant Mechanisms*. Springer Nature Singapore Pte Ltd., 1 ed., 2018.

[17] M. Jin and X. Zhang, "A new topology optimization method for planar compliant parallel mechanisms," *Mechanism and Machine Theory*, vol. 95, pp. 42 – 58, 2016.

[18] J. Wong, L. Ryan, and I. Y. Kim, "Design optimization of aircraft landing gear assembly under dynamic loading," *Structural and Multidisciplinary Optimization*, vol. 57, no. 3, pp. 1357–1375, 2018.

[19] T. Ghandriz, C. Führer, and H. Elmqvist, "Structural topology optimization of multibody systems," *Multibody System Dynamics*, vol. 39, no. 1, pp. 135–148, 2017.

[20] K. Sedlaczek and P. Eberhard, "Topology optimization of large motion rigid body mechanisms with nonlinear kinematics," *Journal of Computational and Nonlinear Dynamics*, vol. 4, no. 2, pp. 021011–021011–8, 2009.

[21] G. H. Yoon and J. C. Heo, "Constraint force design method for topology optimization of planar rigid-body mechanisms," *Computer-Aided Design*, vol. 44, no. 12, pp. 1277–1296, 2012.

[22] H. Wang, W. Uy, and G. Chen, "An approach of topology optimization of multi-rigid-body mechanism," *Computer-Aided Design*, vol. 84, pp. 39 – 55, 2017.

[23] L. W. Funke and J. P. Schmiedeler, "Simultaneous topological and dimensional synthesis of planar morphing mechanisms," *ASME Journal of Mechanisms and Robotics*, vol. 9, no. 2, pp. 021009–021009–9, 2017.

[24] G. H. Yoon and Y. Y. Kim, "Element connectivity parameterization for topology optimization of geometrically nonlinear structures," *International Journal of Solids and Structures*, vol. 42, no. 7, pp. 1983–2009, 2005.

[25] Y. Kim, G. Jang, J. Park, J. Hyun, and S. Nam, "Automatic synthesis of a planar linkage mechanism with revolute joints by using spring-connected rigid block models," *Journal of Mechanical Design*, vol. 129, no. 9, pp. 930–940, 2006.

[26] S. Nam, G. Jang, and Y. Kim, "The spring-connected rigid block model based automatic synthesis of planar linkage mechanisms: Numerical issues and remedies," *Journal of Mechanical Design*, vol. 134, no. 5, pp. 051002–051002–11, 2012.

[27] K. Swartz, D. Tortorelli, and K. James, "Optimal design of multi-body mechanisms using layered connectivity parameterization (lcp)," in *Multidisciplinary Analysis and Optimization Conference*, pp. 1865–1879, AIAA Aviation Forum, 2018.

[28] K. Svanberg, "The method of moving asymptotes- a new method for structural optimization," *International Journal for Numerical Methods in Engineering*, vol. 24, no. 2, pp. 359–373, 1987.

[29] C. Pedersen, T. Buhl, and O. Sigmund, "Topology synthesis of large-displacement compliant mechanisms," *International Journal for Numerical Methods in Engineering*, vol. 50, no. 12, pp. 2683–2705, 2001.

[30] R. W. Ogden, *Non-Linear Elastic Deformations*. Dover Publications, Inc., 1 ed., 1984.

[31] T. E. Bruns and D. Tortorelli, "An element removal and reintroduction strategy for the topology optimization of structures and compliant mechanisms," *International Journal for Numerical Methods in Engineering*, vol. 57, no. 10, pp. 1413–1430, 2003.

[32] H. Kuhn and A. Tucker, "Nonlinear programming," in *Proceedings of 2nd Berkeley Symposium*, pp. 481–492, University of California Press, 1951.